NeuroImage: Clinical 23 (2019) 101921

Contents lists available at ScienceDirect

NeuroImage: Clinical

journal homepage: www.elsevier.com/locate/ynicl

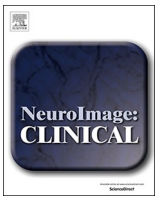

Spatiotemporal trajectories of quantitative magnetization transfer measurements in injured spinal cord using simplified acquisitions

Feng Wang[a,b], Tung-Lin Wu[a,c], Ke Li[a], Li Min Chen[a,b,*,1], John C. Gore[a,b,c,1]

[a] Vanderbilt University Institute of Imaging Science, Vanderbilt University Medical Center, Nashville, TN 37232, USA
[b] Department of Radiology and Radiological Sciences, Vanderbilt University Medical Center, Nashville, TN 37232, USA
[c] Department of Biomedical Engineering, Vanderbilt University, Nashville, TN 37232, USA

ARTICLE INFO

Keywords:
MRI
Quantitative magnetization transfer (qMT)
Pool size ratio (PSR)
Spinal cord injury
Demyelination
Recovery

ABSTRACT

Purpose: This study aims to systematically evaluate the accuracy and precision of pool size ratio (PSR) measurements from quantitative magnetization transfer (qMT) acquisitions using simplified models in the context of assessing injury-associated spatiotemporal changes in spinal cords of non-human primates. This study also aims to characterize changes in the spinal tissue pathology in individual subjects, both regionally and longitudinally, in order to demonstrate the relationship between regional tissue compositional changes and sensorimotor behavioral recovery after cervical spinal cord injury (SCI).

Methods: MRI scans were recorded on anesthetized monkeys at 9.4 T, before and serially after a unilateral section of the dorsal column tract. Images were acquired following saturating RF pulses at different offset frequencies. Models incorporating two pools of protons but with differing numbers of variable parameters were used to fit the data to derive qMT parameters. The results using different amounts of measured data and assuming different numbers of variable model parameters were compared. Behavioral impairments and recovery were assessed by a food grasping-retrieving task. Histological sections were obtained *post mortem* for validation of the injury.

Results: QMT fitting provided maps of pool size ratio (PSR), the relative amounts of immobilized protons exchanging magnetization compared to the "free" water. All the selected modeling approaches detected a lesion/cyst at the site of injury as significant reductions in PSR values. The regional contrasts in the PSR maps obtained using the different fittings varied, but the 2-parameter fitting results showed strong positive correlations with results from 5-parameter modeling. 2-parameter fitting results with modest (> 3) RF offsets showed comparable sensitivity for detecting demyelination in white matter and loss of macromolecules in gray matter around lesion sites compared to 5-parameter fitting with fully-sampled data acquisitions. Histology confirmed that decreases of PSR corresponded to regional demyelination around lesion sites, especially when demyelination occurred along the dorsal column on the injury side. Longitudinally, PSR values of injured dorsal column tract and gray matter horns exhibited remarkable recovery that associated with behavioral improvement.

Conclusion: Simplified qMT modeling approaches provide efficient and sensitive means to detect and characterize injury-associated demyelination in white matter tracts and loss of macromolecules in gray matter and to monitor its recovery over time.

1. Introduction

Traumatic spinal cord injuries (SCI) disrupt the normal functions of the spinal cord, and lead to sensory, motor, and autonomic functional deficits. Injury may induce cell death, and lead to demyelination (Guest et al., 2005; Totoiu and Keirstead, 2005), edema and formation of cysts (Thuret et al., 2006) in the cord tissues over time. Non-invasive quantitative magnetic resonance imaging (MRI) methods are well suited for monitoring the damage to, and recovery of, injured spinal cord tissues, and can provide comprehensive information on structural, functional and molecular changes (Stroman et al., 2014; Wheeler-Kingshott et al., 2014; Chen et al., 2015; Wang et al., 2015; Yang et al., 2015; Wang

* Corresponding author at: Department of Radiology and Radiological Sciences, Vanderbilt University Institute of Imaging Science, AA 1105 MCN, 1161 21st Ave. S., Nashville, TN 37232, USA.
E-mail address: limin.chen@vanderbilt.edu (L.M. Chen).
[1] Equal contribution

https://doi.org/10.1016/j.nicl.2019.101921
Received 15 February 2019; Received in revised form 4 June 2019; Accepted 30 June 2019
Available online 02 July 2019

et al., 2016; Wang et al., 2018a, 2018b). To fully characterize the underlying spontaneous recovery of damaged cords, it is possible to monitor changes in multiple MRI parameters at and around spinal cord lesion sites and ultimately relate these non-invasive MRI measures to the behavioral recovery in monkeys with SCI (Chen et al., 2015; Wang et al., 2015; Wang et al., 2016; Wang et al., 2018a, 2018b). However, for practical applications as imaging biomarkers of pathology, rapid and efficient protocols for acquiring data to derive quantitative MRI parameters are essential.

Among available MRI methods, magnetization transfer (MT) MRI provides information that may be used to detect and grade myelination changes after an injury and during the repair process. MT is the spin exchange between proton pools in different environments and can be used to characterize spatial distributions of the macromolecular and free water proton pools of biological tissues (Wolff et al., 1991a, 1991b, Wolff, Eng et al., 1991). Measurements of the magnetization transfer ratio (MTR) (Wolff and Balaban, 1989) have been used to assess changes in macromolecular composition in neurological disorders (Catalaa et al., 2000; Odrobina et al., 2005), renal disease (Wang et al., 2014), cancer (Quesson et al., 1997), and SCI (Ng et al., 2009; Wang et al., 2015). However, the sensitivity, specificity and reproducibility of MTR measures can be influenced by various experimental parameters such as MT saturation power and RF offset (McGowan 3rd et al., 1994; Ramani et al., 2002; Wang et al., 2018a, 2018b). Moreover, MTR measures tend to reflect a complex combination of exchange and relaxation parameters (Eng et al., 1991; McGowan 3rd et al., 1994), so the interpretation of MTR changes is not always clear.

Quantitative MT (qMT) methods have been developed to measure intrinsic MT parameters to increase specificity and sensitivity. A common approach assumes protons reside in two pools (free water and relatively immobilized in macromolecules) that are coupled by exchange of magnetization. The pool size ratio (PSR, the ratio of the macromolecular proton pool to the free water pool) can be derived from appropriate measurements and is largely independent of relaxation and exchange rates and experimental parameters (Henkelman et al., 1993; Sled and Pike, 2000; Gochberg and Gore, 2003). The pulsed saturation sequence is the most widely adopted qMT method of acquiring data, and various strategies for rapid qMT imaging have been proposed previously (Underhill et al., 2011; Yarnykh, 2012). However, applications of high-resolution qMT mapping of the SC have been challenging (Wang et al., 2016), partly due to the small cord size, relatively low signal-to-noise ratio (SNR) at high resolution, limited data acquisition time, and motion artifacts, including effects caused by cardiac and respiratory cycles and associated cerebral spinal fluid (CSF) pulsation. Furthermore, gross/bulk motion during long data acquisitions may also cause artifacts in the images and introduce biased estimations of qMT parameters. To mitigate these effects, it may be helpful to reduce the amount of qMT data acquired, and to reduce the number of unknown parameters to be fit to the data (Yarnykh, 2012; Smith et al., 2014). In some rapid and simplified approaches (Yarnykh, 2012, Smith et al., 2014), constant values have been assumed for those model parameters that do not show substantial biological variations or to which the fitting results are relatively insensitive.

White matter (WM) is composed predominantly by long-range myelinated axon tracts. Gray matter (GM) is distinguishable from WM in that it contains more numerous cell bodies and relatively few myelinated axons. We have previously shown that fitting the 2-pool model with 5 parameters provides PSR values with high-precision that are sensitive for detecting demyelination in WM and decreases of macromolecules such as proteins in GM of injured spinal cords of non-human primate (NHP) (Wang et al., 2016). The current study aimed to systematically evaluate the accuracy and precision of estimates of PSR from qMT measurements using simplified approaches to data acquisition and analyses for monitoring injury-associated pathological changes in the spinal cords of NHPs. A primary goal was to optimize and evaluate a rapid, robust, sensitive and high-resolution PSR mapping protocol for assessing SCI in primates at high field. The PSR obtained using a fully-sampled data set and a 5-parameter fit to the model of Henkelman and Ramani (Henkelman et al., 1993; Ramani et al., 2002; Cercignani and Barker, 2008; Wang et al., 2016) was used as the reference standard to compare with simplified approaches. We compared the PSR values and their regional correlations for different acquisitions and analyses, and evaluated their reproducibility and sensitivity for detecting tissue composition changes following injury. In addition, we evaluated the performances of each method in detecting injury and repair and their relationships to the behavioral recovery of sensorimotor function of hand over time. Histological analyses of postmortem tissues confirmed the location and extents of tissue pathology. The specific NHP SCI model used shows a close resemblance to human spinal cord injuries (Kaas et al., 2008), which increases the relevance of the simplified qMT acquisition and modeling approaches investigated.

2. Material and methods

2.1. Numerical simulation

Numerical simulations (Cercignani and Alexander, 2006) were performed to test the performances of different modeling approaches and SNR (Sup. Figs. S1-S3). F = 0.1 was used to synthesize qMT data with 12 RF offsets from 1 to 100 kHz at 820° and 220°, with other parameters ($S_0 = 1$, $RM_{0a} = 17.6\,s^{-1}$, $R_aT_{2a} = 0.0184$, and $T_{2b} = 10.5\,\mu s$) adopted from a previous study in normal spinal cords (Wang et al., 2016). Gaussian noise was added to the generated signals, and 1024 noisy data sets for each RF offset at each SNR were synthesized (SNR at 25, 50, 75, 100, and 125 for S_0).

2.2. Animal preparation

Twelve male adult squirrel monkeys (*Saimiri sciureus*) were studied. Eight of them underwent a unilateral dorsal column transection at cervical level 5 (C5). These monkeys were scanned before and after SCI. The specific scan time points varied slightly across animals (about 2, 4, 6, 8, 10, 12, 14, 16 or 24 weeks), depending on the behavioral recovery of each subject. Throughout the entire MR imaging session, each monkey was anesthetized (isoflurane 0.5–1.5%) and mechanically ventilated (40 respiration cycles/min), with head and body stabilized in an MR-compatible frame. Vital signs, including core body temperature, heart rate, respiration rate, SpO_2, and end-tidal CO_2, were monitored and maintained at a stable level. All procedures followed NIH guidelines on the care and use of laboratory animal.

2.3. In vivo MRI

All MRI data were acquired on a Varian DirectDrive™ horizontal 9.4 T scanner using a saddle-shaped transmit-receive surface coil positioned around the cervical spine region. The image field of view was centered at the level where the lesion was targeted. The MRI acquisition protocol was similar to that employed in our previous study (Wang et al., 2016) and details are provided in the supporting information. After acquiring high resolution structural images with magnetization transfer contrast (MTC) to guide the placements of image slices, qMT data were obtained from a coronal slice where the dorsal columns and dorsal horns reside (Fig. 1A–C) using a 2D MT-weighted spoiled gradient echo sequence (TR 24 ms, flip angle =7°, resolution = ~$0.313 \times 0.313 \times 1$ mm^3). We obtained qMT data using 12 different RF offsets (Fig. 1E) between 1 and 100 kHz and two saturation powers (θ_{sat} = 220° and 820°, pulse width = 12 ms).

2.4. Data analyses

All MRI data were analyzed using MATLAB (The Mathworks). The detailed procedures for data analyses are presented in the supporting

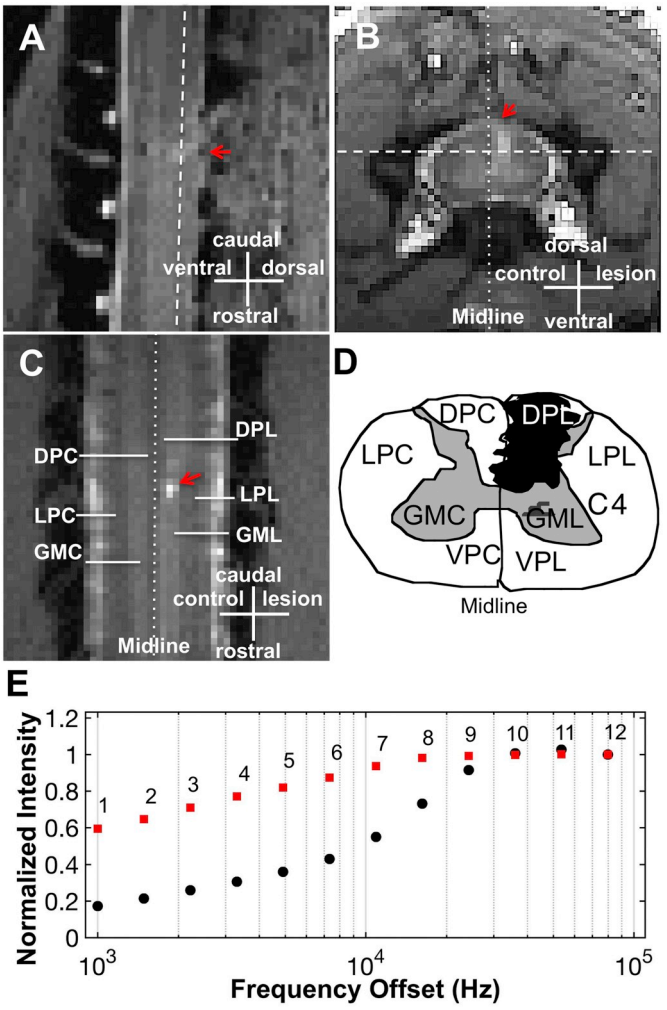

Fig. 1. Quantitative MT imaging of cervical spinal cord with a unilateral dorsal column lesion. (A-C) Sagittal, axial and coronal images with MT contrast. The arrows indicate the lesion site. White dashed lines indicate the location of coronal imaging plane. DPC (dorsal pathway), LPC (lateral pathway), VPC (ventral pathway) and GMC (gray matter) are on the non-lesion control side; DPL, LPL, VPL and GML indicate respective regions on the lesion side. (D) Schematic illustration of the reconstructed lesion of dorsal column on the right side (black patch). (E) MT *in vivo* data showing the normalized intensity extracted from normal spinal cord GM at different RF offsets and two flip angles of θ_{sat} 820° (black circles) and 220° (red squares).

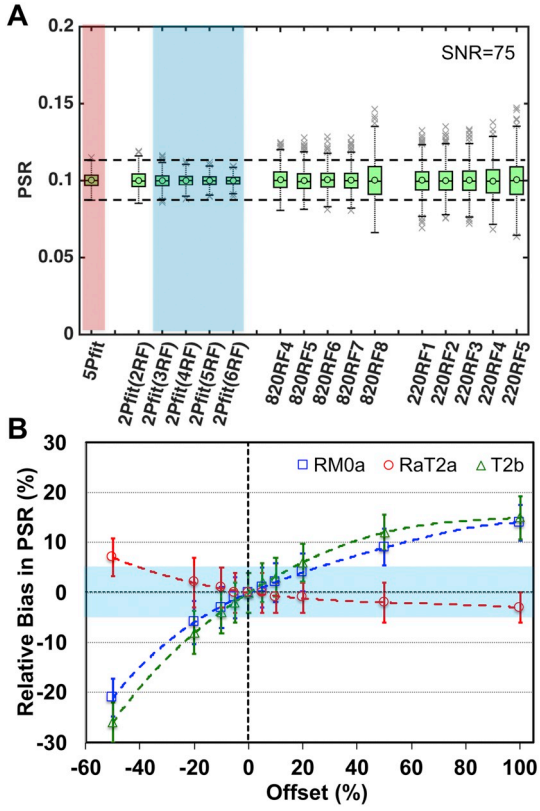

Fig. 2. Accuracy and precision of PSR estimated from numerical simulations. (A) Boxplots of PSR from selected analytic approaches. Simulated qMT data were generated with PSR = 0.1 and SNR = 75 for S_0 (N = 1024). The circles and middle lines represent mean and median values respectively (N = 1024). Measures using 2Pfit with comparable or less variations than those using 5Pfit are shaded in blue. (B) Relative bias in PSR when the actual RM_{0a}, R_aT_{2a} or T_{2b} is different from the fixed reference value in 2-parameter modeling (4 RF offsets). The black dotted line represents the fixed reference for all analyses. Error bars represent standard deviations. Bias < 5% is shaded in blue.

information.

QMT parameters M_0, F, RM_{0b}, T_{2a} and T_{2b} were first determined from the 5-parameter fitting (= 5Pfit) using the fully sampled qMT data, based on the model of Henkelman and Ramani (Ramani et al., 2002; Cercignani and Barker, 2008).

$$SI(\omega_1,\Delta f)=\frac{M_0\left(R_b\left[\frac{RM_{0a}F}{R_a}\right]+R_{RFB}\left(\omega_{1CWPE},\Delta f,T_{2b}\right)+R_b+RM_{0a}\right)}{\left[\frac{RM_{0a}F}{R_a}\right]\left(R_b+R_{RFB}\left(\omega_{1CWPE},\Delta f,T_{2b}\right)\right)+\left(1+\left[\frac{\omega_{1CWPE}}{2\pi\Delta f}\right]^2\left[\frac{1}{T_{2a}R_a}\right]\right)\left(R_{RFB}\left(\omega_{1CWPE},\Delta f,T_{2b}\right)+R_b+RM_{0a}\right)} \quad (1)$$

where ***a*** and ***b*** denote the free water and macromolecular pools, respectively. F is the relative size of the macromolecular pool, defined as $F = M_{0b}/M_{0a}$. M_{0a} and M_{0b} are the fully relaxed values of magnetization associated with the two pools, and M_0 is the signal without MT-weighting. The continuous wave power approximation (CWPE) was applied and ω_{1CWPE} is the amplitude of the saturating field (Ramani et al., 2002, Cercignani and Barker, 2008). Δf represents the frequency offset of the MT pulse. R_{RFB} is the rate of saturation of longitudinal magnetization in pool ***b*** due to the irradiation by the amplitude defined by ω_{1CWPE} and Δf (Cercignani and Barker, 2008), which is also dependent on the transverse relaxation time of the macromolecular pool T_{2b}. R is the exchange rate constant between the two pools. R_a and R_b are the respective pool longitudinal relaxation rates. More details were described in a previous study (Wang et al., 2016) and in the supporting information. The PSR was defined as the value of F from this fitting. We used the root mean squares (RMS) of the residuals to evalute the fitting quality at each pixel.

It has been demonstrated that the exchange rate RM_{0a} is not very sensitive to pathophysiological changes in tissues even though M_{0a} may vary by several % (Smith et al., 2009; Underhill et al., 2011) and so can be assumed to be constant. T_{2b} also varies little between tissues as their macromolecular protons are immobilized to similar degree, and it can also be assumed as a constant (Sled and Pike, 2001; Yarnykh and Yuan, 2004). Although R_a and T_{2a} may both vary significantly, the variation of their product is relatively small in both healthy and diseased tissues, so that R_aT_{2a} can be assumed to be constant (Yarnykh and Yuan, 2004). These assumptions were also found reasonable for observations around lesions in injured monkey spinal cords (Wang et al., 2016). Thus, three parameters RM_{0a}, T_{2b} and R_aT_{2a} could be held constant during fitting, based on respective median values from normal spinal cords (17.6 s^{-1}, 10.5 μs, and 0.0184). Then there are only two remaining parameters, M_0 and F, to be estimated. These may be derived using selected numbers of RF offsets. In this work, 2Pfit represents 2-parameter fitting

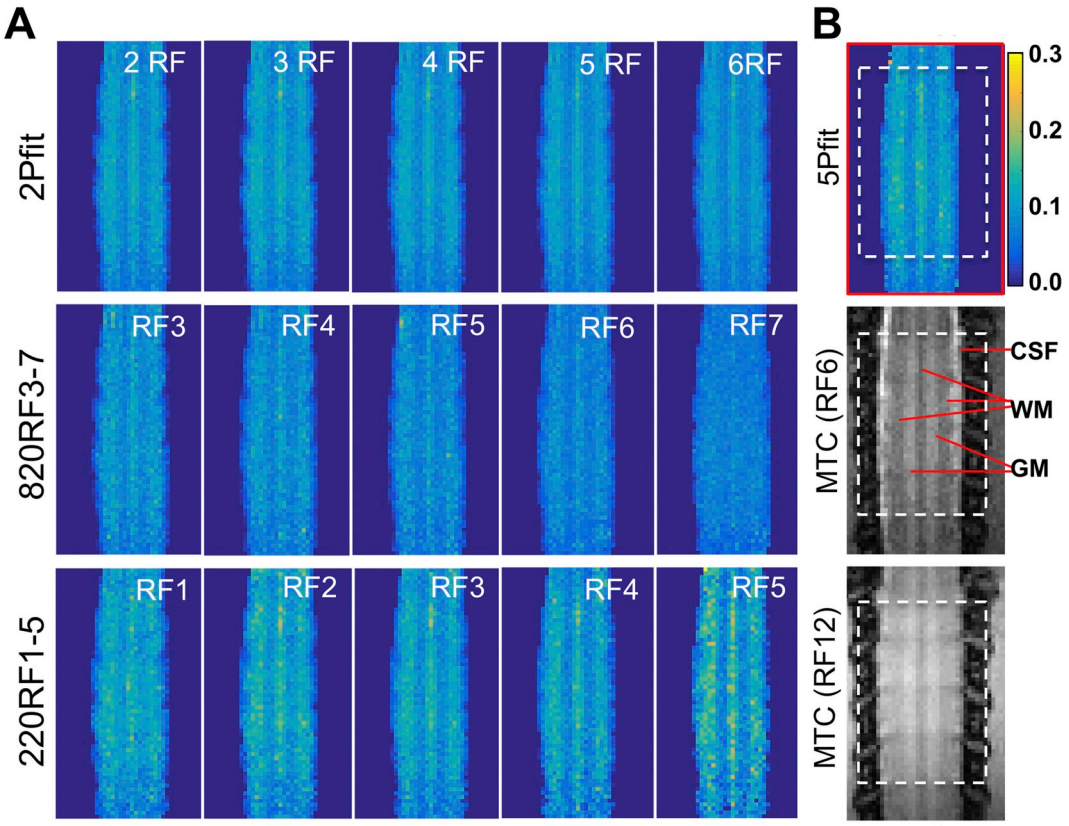

Fig. 3. Comparison of PSR maps derived from different modeling approaches in normal spinal cord of one representative subject. (A) Representative PSR maps showing 2-parameter fitting (2Pfit) using 2 to 6 RF offsets, 1-parameter calculation based on selected RF offset (RF3–7) and RF12 at 820° (820RF3–7), and 1-parameter calculation based on data with selected RF offset (RF1–5) and RF12 at 220° (220RF1–5). (B) Raw MTC images and PSR map showing 5-parameter fitting (5Pfit) using data with 12 RF offsets at 820°. Pixels in the box, restricted to a B_0 and B_1 homogeneous region, were included in further regional analysis.

results using between 2 and 6 RF offsets. 2Pfit(2RF) uses measured offsets #4 and #12, 2Pfit(3RF) used #3, #4 and #12, 2Pfit(4RF) used #2-#4 and #12, 2Pfit(5RF) using #2-#5 and #12, and 2Pfit(6RF) using #2-#6 and #12, respectively (Fig. 1E). The selection of these sampling pairs was based on numerical simulations (Sup. Fig. S3).

In the special case that one of the two sampling points is at a very large frequency offset (S_0), the saturation effect can also be ignored, and S_0 can be used to normalize the other measured data at lower frequency offsets (S_n) so the corresponding F/R_a may be written as:

$$\frac{F}{R_a} = \frac{(R_{RFB}(\omega_{1CWPE}, \Delta f, T_{2b}) + R_b + RM_{0a})\left(1 - S_n\left(1 + \left[\frac{\omega_{1CWPE}}{2\pi\Delta f}\right]^2\left[\frac{1}{T_{2a}Ra}\right]\right)\right)}{RM_{0a}(S_n(R_{RFB}(\omega_{1CWPE}, \Delta f, T_{2b}) + R_b) - R_b)} \quad (2)$$

Direct 1-parameter estimates with different RF offset pairs are denoted by the other selected RF offset *e.g.* 820RF4 (#4 and #12), 820RF5 (#5 and #12), 820RF6 (#6 and #12), 820RF7 (#7 and #12) and 820RF8 ((#4 and #12) for data obtained with $\theta_{sat} = 820°$, and 220RF1 (#1 and #12), 220RF2 (#2 and #12), 220RF3 (#3 and #12), 220RF4 (#4 and #12), and 220RF5 (#5 and #12) for data using $\theta_{sat} = 220°$. The selection of these sampling pairs was also based on numerical simulations (Sup. Fig. S3).

High-resolution MTC images were referenced for manual selection of ROIs (regions of interests) for quantification, including WM in dorsal pathway, lateral pathway, and GM on both the lesion and control side, and cyst/lesion (Fig. 1C). Only regions with homogeneous B_0 and B_1 ($|\Delta B_0| < 100$ Hz, and $|\Delta B_{1ratio}| < 0.05$) were selected and included in the ROI analysis (< 1.5 cm in length) (Wang et al., 2018a, 2018b). To minimize partial volume effects, small ROIs were selected and voxels residing along the SC – CSF border were excluded. The normal PSR range was defined as the mean value ± 2SD (standard deviation, 95%) of the normal tissues of the respective region (WM in dorsal pathway or lateral pathway, and GM) in the normal spinal cord, and an abnormal tissue (AT) region was defined as those voxels with PSR out of the normal range. Contrasts between WM and GM were evaluated by $(PSR_{max}\text{-}PSR_{min})/(PSR_{max} + PSR_{min})$, where PSR_{max} and PSR_{min} were the maximum PSR of WM and minimum PSR of GM respectively. Correlations were calculated using the Pearson correlation function. The significance of measurement differences was evaluated using Student's *t*-tests, and FDR (false discovery rate) corrected $p < 0.05$ was considered as significant.

2.5. Dorsal column section and behavioral assessment

In brief, under surgical level of anesthesia and aseptic conditions, the dorsal portion of the lower cervical spinal cord at C4-C6 level was exposed. The dorsal column pathway (tract) was transected on one side with a pair of fine surgical scissors at the C5 level. Each lesion was 2 mm deep and ran from the midline to the spinal nerve entering zone (~ 2 mm in width). Dura was replaced with a small piece of gelfilm, and the wound was closed. Analgesics were administered post-surgically and standard post-surgery care was performed. The details of the surgical procedures can be found in previous publications (Qi et al., 2011; Chen et al., 2012; Qi et al., 2016). The detailed procedures for behavioral assessment are described in the supporting information.

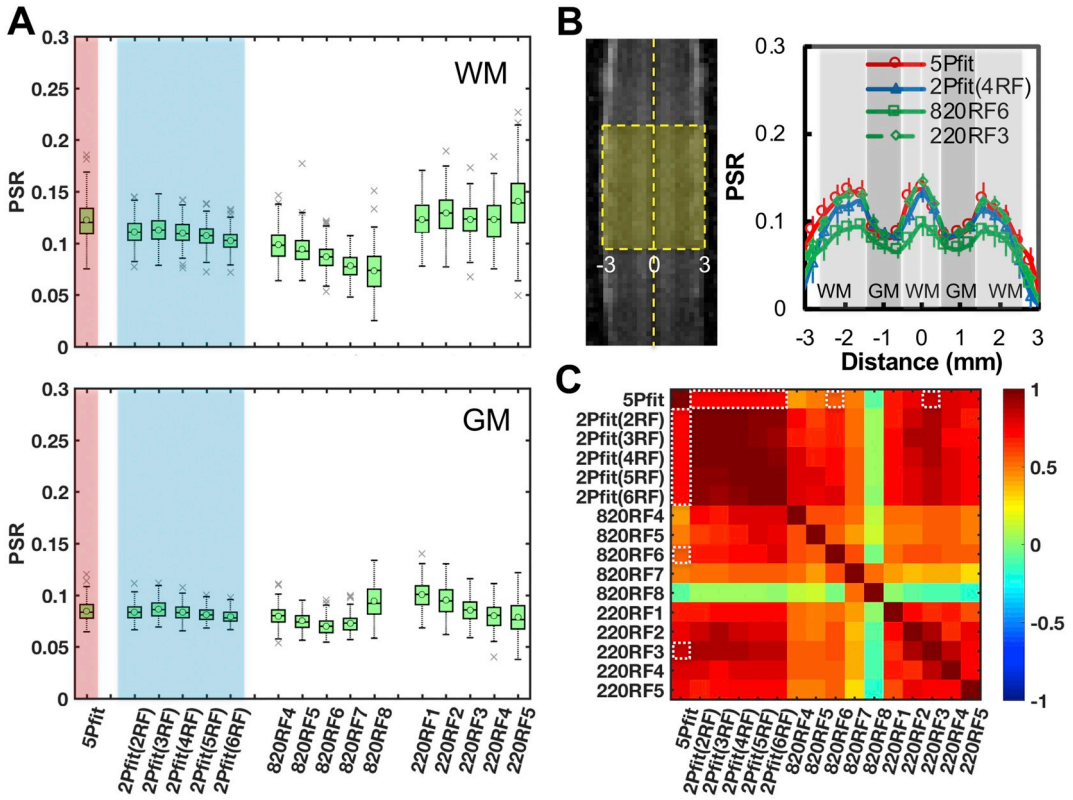

Fig. 4. Comparison of regional PSR distributions in normal spinal cord of one representative squirrel monkey. (A) Boxplots of regional PSR of WM and GM from selected analytic approaches. The circles and middle lines represent mean and median values respectively. The crosses indicate outliers. Measures of WM and GM from simplified modeling approaches with comparable accuracy and less variations than those using 5Pfit are shaded in blue. (B) Profiles from selected modeling approaches, showing the PSR distributions across spinal cord transversely. The error bars indicate the standard deviation across voxels along the longitudinal direction in the box shown in plot B. The midline between the lesion and non-lesion sides is indicated by the dashed line (Distance = 0). (C) 2D matrix plot of correlation coefficients between all PSR measures ($p < .05$ for all). The relatively stronger correlations to 5Pfit are indicated by the white dotted boxes.

2.6. Histology

Silver stains of post-mortem tissue (40-μm thickness) were used to evaluate the segmental level and spatial extent of each spinal cord lesion and the degree and extent of demyelination, and to confirm the spatial extents of qMT-derived PSR measures at the end stage of recovery. Histological sections in the same orientation as qMT data acquisitions were obtained from three subjects, while all the other subjects were used to obtain sections transverse to spinal cords to allow validation of other MRI results from diffusion and functional MRI.

3. Results

3.1. Numerical simulation and potential bias with incorrect parameter assumptions

The performances of different qMT data analyses were systematically evaluated for simulated data. Higher SNR and a larger number of RF offsets can significantly reduce experimental errors and variance of qMT model fits (Sup. Figs. S1-S3). Due to the experimental SNR range in this study, we adopted acquisition of at least 10 RF offsets for 5-parameter fitting (Wang et al., 2016). Considering the potential for degrading motion effects in the *in vivo* studies, we acquired *in vivo* qMT data with 12 RF offsets (Fig. 1E). From the comparison of simulated results using different modeling approaches (Fig. 2A and Sup. Fig. S2), at least 3 RF offsets are required in 2-parameter fitting to retain comparable accuracy and precision as that obtained from 5-parameter fitting with 12 RF offsets, at the same SNR level. 1-parameter calculations require higher SNR (> 1.5 times) to approach comparable accuracy and precision as 5-parameter fitting with 12 RF offsets (Sup. Fig. S2). The 1-parameter calculations are very sensitive to RF offset and power, but the optimum offset and power can be determined (Sup. Figs. S2-S3). The sampling pairs of (820°, 5–7 kHz) yielded the most accurate and precise estimates of PSR (Fig. 2A and Sup. Figs. S2-S3). However, the 1-parameter approach using sampling pairs at 220° did not provide comparable precision and accuracy compared to other approaches at the same SNR level, and the optimum RF offset range is much narrower than that for 1-parameter estimates using data at 820° (Sup. Fig. S3B). From the comparison of 1-, 2-, and 5-parameter approaches at different SNR levels (Fig. 2A and Sup. Fig. S2), the 2-parameter fitting (#RF offsets > 2) approach showed greater robustness than the 5-parameter approach using 12 RF offsets, as revealed by greater accuracy with no loss of precision with correct parameter assumptions for RM_{0a}, T_{2b} and R_aT_{2a}.

Relative biases in PSR values were estimated for 2-parameter fitting (Fig. 2B). The bias in the estimated PSR value was dependent on the deviation of the selected and the true reference values of RM_{0a}, T_{2b} and R_aT_{2a}.

3.2. In vivo PSR of normal spinal cord from different approach

Representative PSR maps of normal spinal cord from simplified fittings are compared to a PSR map obtained by 5-parameter fitting in Fig. 3. 2-parameter PSR maps showed better precision than the 5-parameter result (Fig. 4A), and contrasts between WM and GM were maintained (Figs. 3-4). The voxel-based profiles of PSR values across

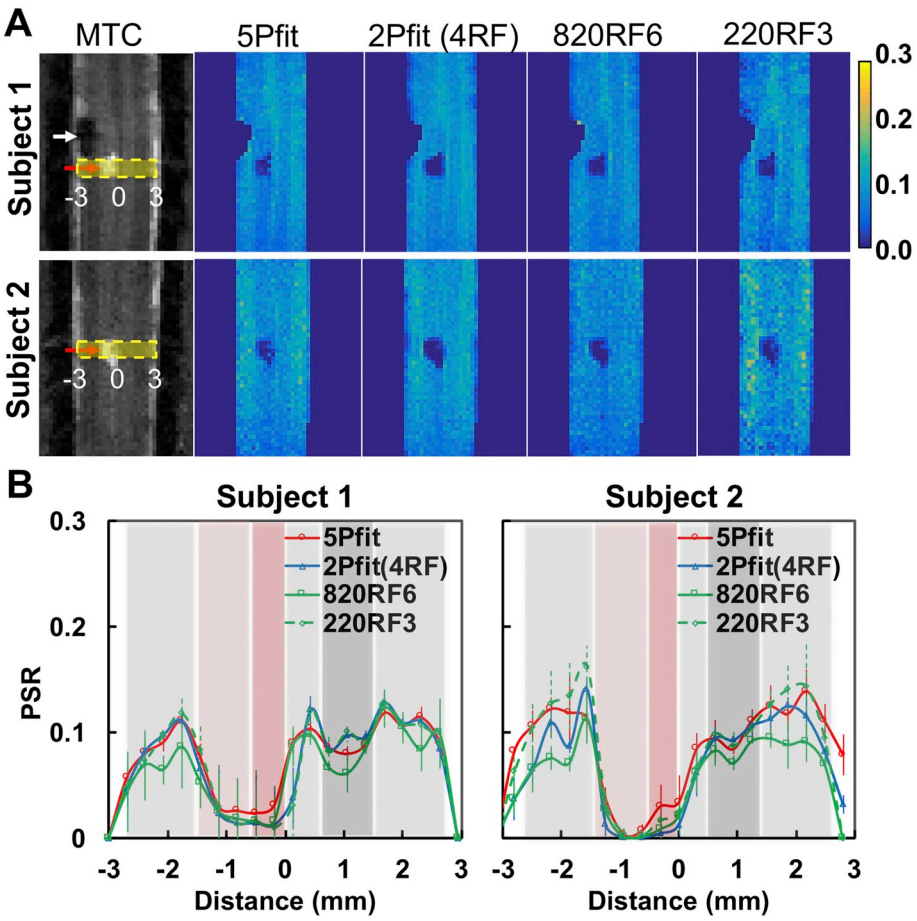

Fig. 5. Comparison of PSR of injured spinal cord from selected modeling approaches. (A) Representative PSR maps from two subjects showing 5-parameter fitting 5Pfit, 2-parameter fitting 2Pfit (4RF), 1-parameter calculations 820RF6 and 220RF3. (B) Profiles from selected modeling approaches, showing the PSR distributions across spinal cord transversely at the lesion level (yellow stripe shown in plot A). The error bars indicate the standard deviation across voxels along the longitudinal direction in the yellow stripe. The midlines between the lesion and non-lesion sides are indicated by Distance = 0.

WM-GM-WM-GM-WM strips (Fig. 4B) illustrated that contrasts between WM and GM were comparable for 5Pfit, 2Pfit(4RF), and 220RF3, but weaker for 820RF6. The contrasts between PSRs of WM and GM were 0.239, 0.217, 0.144 and 0.260 for 5Pfit, 2Pfit(4RF), 820RF6 and 220RF3 respectively. While the contrast between PSRs of WM and GM from 2Pfit was slightly lower than that from 5Pfit, the PRS values across voxels in WM or GM from 2Pfit showed higher precision than those from 5Pfit, indicated by less variability (Fig. 4A-B). All 2Pfit results showed strong correlations ($r > 0.7$) with the 5Pfit result in general (Fig. 4C). In addition, the averaged PSR values of WM and GM from 2-parameter fitting are close to those from 5-parameter fitting, with their difference smaller than 5%. 2Pfit of WM showed larger variance and bias than 2Pfit of GM (Fig. 4A), with doubled standard deviations across voxels. While the values of RM_{0a}, R_aT_{2a} and T_{2b} chosen for these analyses were derived from normal spinal cord data (Wang et al., 2016), the particular choices of these parameters did not introduce a significant source of bias in the PSR estimates of normal tissues. The PSR of WM could be slightly underestimated while that of GM could be slightly overestimated (Figs. 3-4) using 2-parameter fitting. Across subjects, 2-parameter fitting also showed more similar and reproducible PSR maps than 1-parameter fitting (Sup. Fig. S4).

While most simplified 1-parameter approaches showed significant contrast between WM and GM in the PSR maps (Fig. 3A), 820RF7 showed evident loss of contrast. Moreover, though some 1-parameter fits showed high regional correlations with results of 5Pfit (Fig. 4C), their precision and accuracy were not comparable to PSR measures using 2-parameter fitting (Fig. 4A). The variations from 1-parameter measures were large across RF offsets and saturation powers given the experimental SNR (~75), showing negative and positive bias for 820° and 220° respectively (Fig. 4A). Among 1-parameter approaches, 820RF6 and 220RF3 showed the strongest correlations (r values at 0.557 and 0.824) with 5Pfit data at saturation powers 820° and 220° respectively (Fig. 4C).

3.3. PSR changes around the lesion site

5-parameter fitting detected the lesion/cyst and unilateral demyelination below and above the injury site (Fig. 5A). While all the selected 1- and 2- parameter approaches detected the lesion/cyst as a drastic change in PSR at the site of injury (Fig. 5A), 2-parameter approaches mapped the decrease of PSR better than 1-parameter approaches. Furthermore, the regional contrasts in PSR maps from the different approaches varied (Fig. 5A-B), with 2Pfit showing consistent strong positive correlations with 5Pfit (Sup. Fig. S5). The variations from 1-parameter measures were large across RF offsets, powers and subjects (Fig. 5A-B), and 820RF6 and 220RF3 showed relatively stronger correlations (r values at 0.829 and 0.896 for subject 1, and 0.528 and 0.685 for subject 2) with 5Pfit results than measures using other selected RF offsets for 1-parameter modeling (Sup. Fig. S5). Although there were minor differences between the 5Pfit and 2Pfit maps, the overall spatial correspondence of the lesion and magnitude of the estimated PSR changes were similar (Fig. 5A).

3.4. Histology confirmed regional demyelination detected by PSR

Subsequent silver staining confirmed that reduced values of PSR

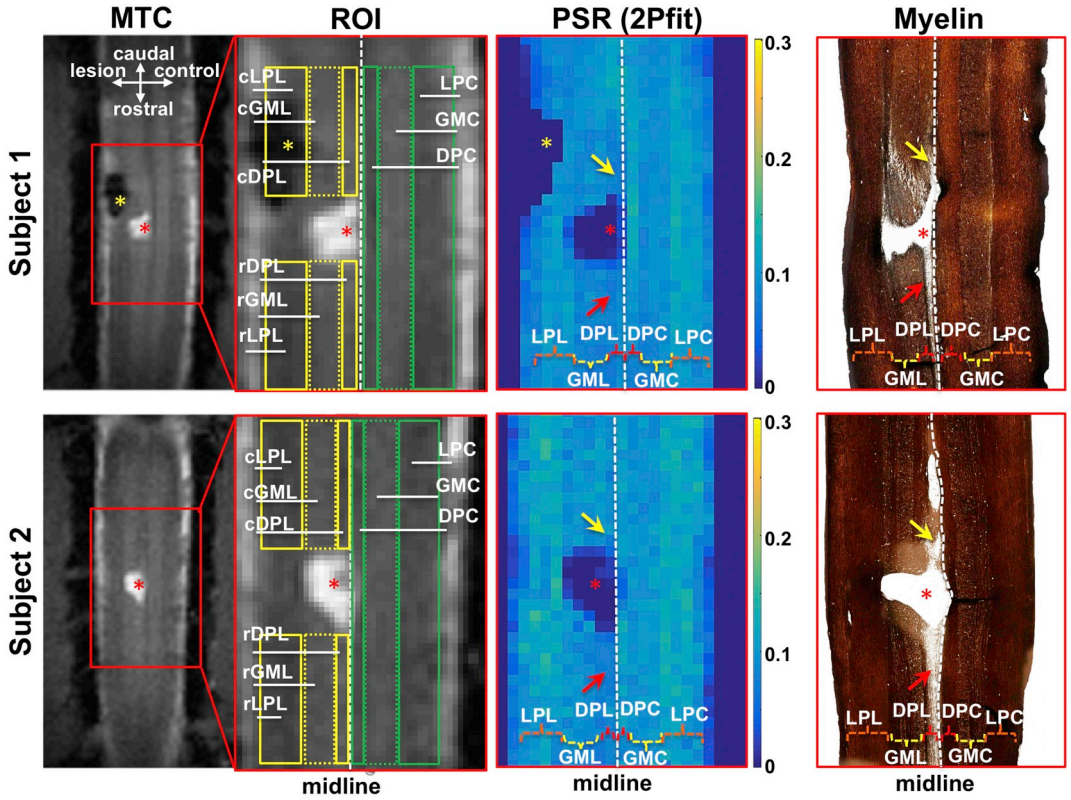

Fig. 6. Spatial correspondences among anatomical images, PSR maps and spinal cord tissues stained with myelin in two representative monkeys. The selected ROIs overlaid on the anatomical images are shown in green and yellow. DPC (dorsal pathway), LPC (lateral pathway), and GMC (gray matter) are on the control side; rDPL, rLPL, and rGML indicate respective regions rostral to the lesion site; cDPL, cLPL, and cGML indicate respective regions caudal to the lesion site. Red asterisks indicate lesion/cyst site, and arrows indicate the unilateral demyelination in the dorsal pathway on the lesion side, both caudal and rostral to the lesion site. Region of filling tissues was excluded from comparison due to the signal void in MRI data, which might be from hemorrhage (yellow asterisks). PSR maps derived from 2-parameter fitting 2Pfit(4RF) are shown for comparison.

spatially corresponded to regional demyelination along the dorsal column WM track on the injury side (Fig. 6). Demyelination was seen mainly on the injured side. Typically, the demyelinated WM tissues spread about 3 mm in length on both caudal or rostral sides to the lesion site, which corresponds to one spinal segment in this species. Along the dorsal column tract, the rostral side (to the lesion) showed more severe demyelination than the caudal side (see red and yellow arrows in Fig. 6). The spatial territory of demyelination in WM and decreases of macromolecular components shown in the silver stain was in general agreement with the regions with low PSR, which were well detected by either 5-parameter fitting or 2-parameter approach (Figs. 5-6).

3.5. Comparison of regional characteristics of PSR measures of injured spinal cord derived from different model fittings

The characteristics of PSR measures obtained from six selected ROIs surrounding the core lesion site were quantified across eight injured subjects, and the results on the lesion sides were compared with the values on the non-lesion side (Fig. 7). We selected six ROIs, caudal and rostral to the cyst/lesion on the injury side (Fig. 6). The lateral pathway (LPC), dorsal horn GM (GMC) and dorsal pathway (DPC) on the non-lesion side were used as reference regions. PSR decreased by different degrees in cysts and tissues around the lesion side (change in cyst > DPL > GML > LPL). The optimum 2- and 1-parameter approaches were very sensitive for detecting cysts, while decreases of PSR in GM were not as significant as in the dorsal WM tracks (Fig. 7A-B). Overall, 2Pfit (#RF offsets > 3) provided comparable sensitivity as 5Pfit to detect regional demyelination of the dorsal column pathway and the loss of macromolecules in the dorsal horn GM around the injury site (Fig. 7A). 1-parameter modeling 820RF3 was less sensitive than 5Pfit (Fig. 7A). Even though 220RF3 showed comparable detectability as 5Pfit, higher SNR is required to improve the precision (Figs. 3–5 and Sup. Fig. S4). Among the regions of abnormal tissues, PSR showed the highest sensitivity for detecting demyelination in dorsal pathway rostral and caudal to the cyst/lesion sites (Fig. 7A-B). The overall agreement between PSR measures from 2Pfit(4RF) and 5Pfit was evaluated *via* correlations and Bland-Altman analyses (Fig. 7C). The PSR measures from 2Pfit(4RF) are proportional to those from 5Pfit ($r = 0.927$, $p < .05$), except in cyst regions (Fig. 7C). In Bland-Altman plots, most cysts show differences below the mean difference between 2Pfit(4RF) and 5Pfit (Fig. 7C), indicating potential bias from 2Pfit(4RF) for evaluating PSR of cyst.

3.6. Longitudinal changes of regional PSR after dorsal column lesion

Serial MT imaging of the same subject revealed temporal changes in structural features and PSR values over time after injury (Fig. 8 and Sup. Fig. S6). We compared regional PSR values derived from 5Pfit, 2Pfit(4RF), 820RF3 and 220RF4. To simplify the longitudinal comparison, we quantified PSR at three time points after injury: the onset point (OP, 1–2 weeks after injury), progression point (PP, 3–5 weeks after SCI), and end point (EP, 6–24 weeks after injury) after SCI. The 2Pfit(RF4) is more robust to noise than 5Pfit (Fig. 8 and Sup. Fig. S6). The 2Pfit(RF4) detected temporal changes in demyelination and

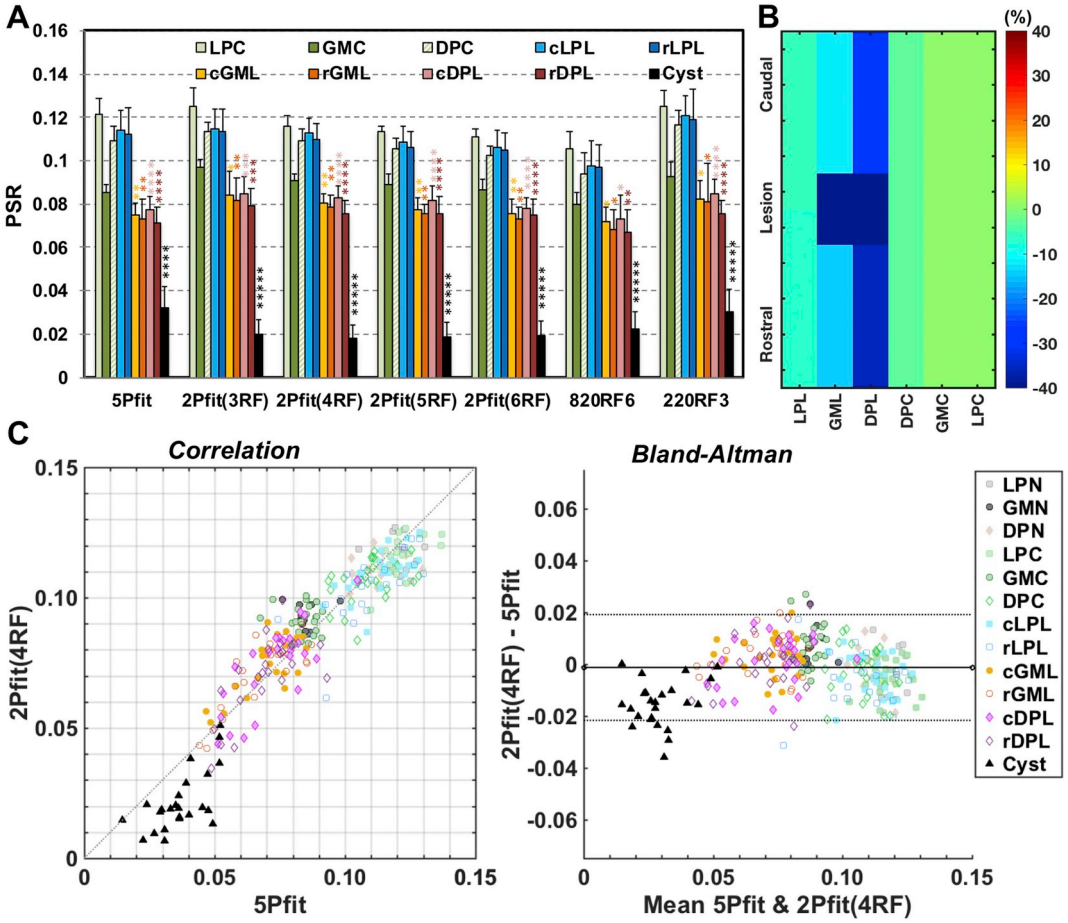

Fig. 7. Comparison of regional PSR of injured spinal cord across subjects ($N = 8$). (A) The regional averaged PSR across subjects derived from different modeling approaches (see Fig. 6 for ROI definition). The bars represent standard deviations. *p < 0.05, **p < .0110^{-2}-2-2, ***p < 10^{-3}-3, ****p < 10^{-4}-4, and *****p < 10^{-5}-5 *vs.* the values of relative regions on the control side. The PSR measures from the end time point (EP) in the longitudinal MRI study were included for quantification. (B) Schematic illustration of the regional percent changes in PSR measures compared to relative regional values of normal tissues from 5Pfit. (C) The comparison of regional PSR measures between 5Pfit and 2Pfit(4RF). In the Bland-Altman plot, solid line represents the mean difference between measures from the two approaches, whereas the dotted lines are 95% limits of agreement.

recovery after injury, as well as 5Pfit (Figs. 8-9). Among all the tissue ROIs, the dorsal column pathway on the lesion side showed the most severe damage (Fig. 7 and Fig. 10) as expected, and all the damaged tissue ROIs showed recovery to different degrees at the end of study (Fig. 10 and Sup. Fig. S7).

3.7. Correlations between PSR and the behavioral measures

Lastly, we examined the relationships between the regional PSR values and behavioral assessments of hand use impairment (*i.e.*, success rate and number of flexes on food retrieval). Fig. 11 shows the observed quantitative correlations (4 subjects with both qMT and behavioral measures included). Two behavior measures of success rate (R) and number of flexes (N) showed drastic behavioral impairments and recovery after injury. The most severe deficits (Fig. 11A), indicated by significant drops of R and increases of N needed to retrieve a food pellet, were highly associated with the minimum PSR of injured tissues (Fig. 9). In general, the PSR correlated positively with the success rate, but negatively with the number of flexes (Fig. 11B). Significant correlations were detected consistently between PSR of dorsal column pathway on the lesion side (cDPL and/or rDPL) and successful rates from wells 1 and 2, using 5Pfit and 2Pfit(RF4). Significant correlations were also detected between PSR of dorsal horn on the lesion side (cGML and/or rGML) and behavioral measures using 2Pfit(RF4). These regions also exhibited stronger linear correlations between PSR changes and behavioral recovery (Sup. Fig. S8).

4. Discussion

4.1. Bias level of PSR measures with 2-parameter approach

We found that an appropriate, simplified, 2-parameter approach was capable of detecting regional demyelination of WM tracts and reductions in macromolecular content in GM surrounding a lesion site with accuracy and precision that are comparable to the full 5-parameter approach (Fig. 7). However, the 2-parameter approach underestimated the PSR values at the lesion/cyst site compared to 5Pfit (Fig. 7). The potential source of bias in the 2-parameter approaches arises from the use of fixed, median values of RM_{0a}, $T_{2a}R_a$, and T_{2b}, obtained from normal spinal cord tissues (Fig. 2B), which ignores the heterogeneity of GM, WM and abnormal tissues. However, the product of R_a and T_{2a} does not alter much in practice (Yarnykh, 2012; Smith et al., 2014; Li et al., 2015). In addition, simulations show that incorrect values of R_aT_{2a} introduce little bias (Fig. 2B). Similarly, simulations predict that

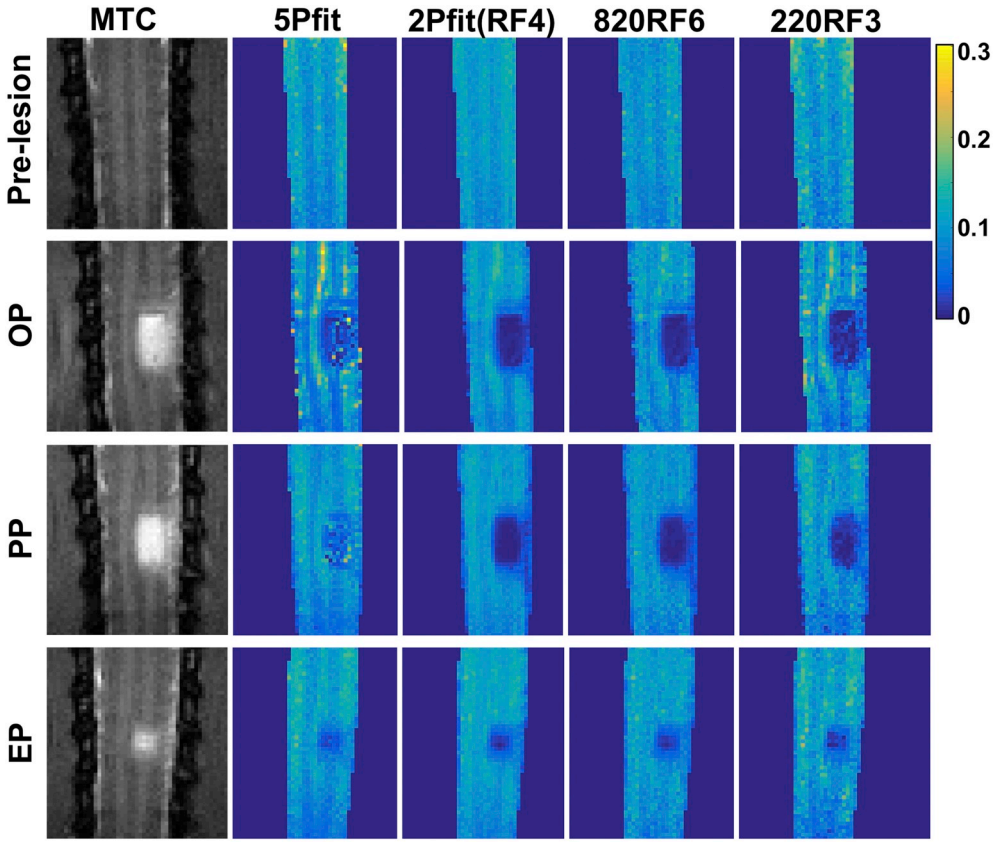

Fig. 8. Longitudinal changes of PSR maps after injury with selected modeling approaches. PSR maps generated from one representative subject with severe injury. Corresponding structural MTC images are shown as references. The stage when cyst occurred was defined as onset point (OP), the progression stage was defined as progression point (PP), the end time point is the last time point in the longitudinal MRI study (EP).

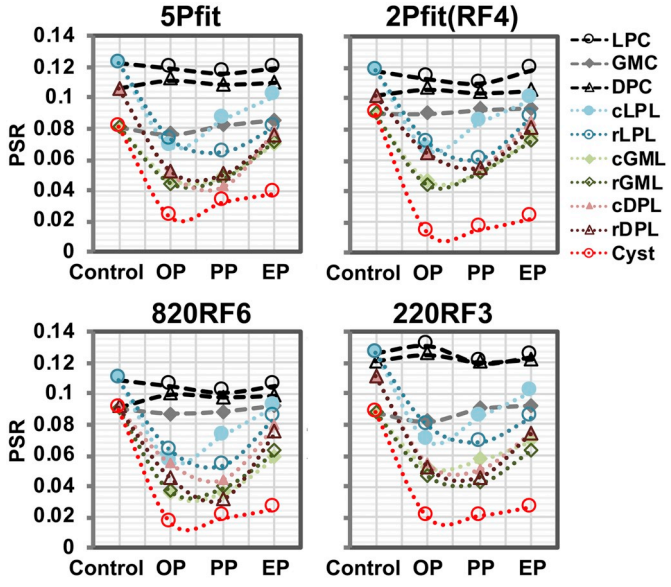

Fig. 9. Individual longitudinal changes of regional averaged PSR measures after injury using selected modeling approaches. PSR measures at different stages were generated from the subject shown in Fig. 8. Pre-lesion results were used as controls. Please see Fig. 6 for ROI definition.

incorrect values of RM_{0a} (± 10%) in abnormal tissues (Wang et al., 2016) around the lesion site will affect estimates of PSR by < 5%. On the other hand, a 50% error in RM_{0a} will result in ~20% bias in the observed PSR, or an underestimation of ~0.02 for PSR of 0.1 (Fig. 2B). Overall, we do not expect incorrect assumptions of values for RM_{0a}, R_aT_{2a} and T_{2b} are a significant source of bias in estimating PSR of normal or abnormal tissues. Our results also showed low levels of bias in the measured values of PSR (Fig. 3, Fig. 4, Fig. 5 and Fig. 7), when the 2-parameter fitting was used. However, cysts formed around the lesion site can have very different values of RM_{0a}, R_aT_{2a}, and T_{2b} (Wang et al., 2016), which then do cause underestimates of PSR in those regions.

4.2. Influence of SNR on the qMT modeling of injured spinal cord

Among 1-, 2- and 5-parameter qMT fitting approaches, a 1-parameter approach is the most sensitive to random motions and noise in the *in vivo* studies. The effect of SNR is particularly strong at low SNR levels, and 5-parameter fitting could be also affected at the early stage after the injury (Fig. 8 and Sup. Fig. S6) when SNR could be affected by neck swelling, bleeding, and other physiological conditions. The greatest reductions in the variability of the *PSR* estimates were identified in WM (Figs. 3-4) using 2-parameter fitting, where the SNR values are the lowest and motion artifacts may be most severe due to the adjacent CSF. From optimization studies (Fig. 2 and Sup. Figs. S2-S3), the MT-weighted image needs to be acquired at relatively high irradiation power and low frequency offset, such as RF offset 4–8 kHz at $\theta_{sat} = 820^{\circ}$ at 9.4 T. When low saturation power is applied, much lower RF offsets must be acquired to reduce the variability (Fig. 2 and Sup. Fig. S2-S3). The 2-parameter fitting uses a broader range of RF offsets for more robust PSR measures (Fig. 2 and Sup. Figs. S2-S3). With the assumption of three additional constants, the 2-parameter modeling (#RF > 3) is more robust to noise than 5-parameter modeling using 12 RF offsets (Figs. 2–4).

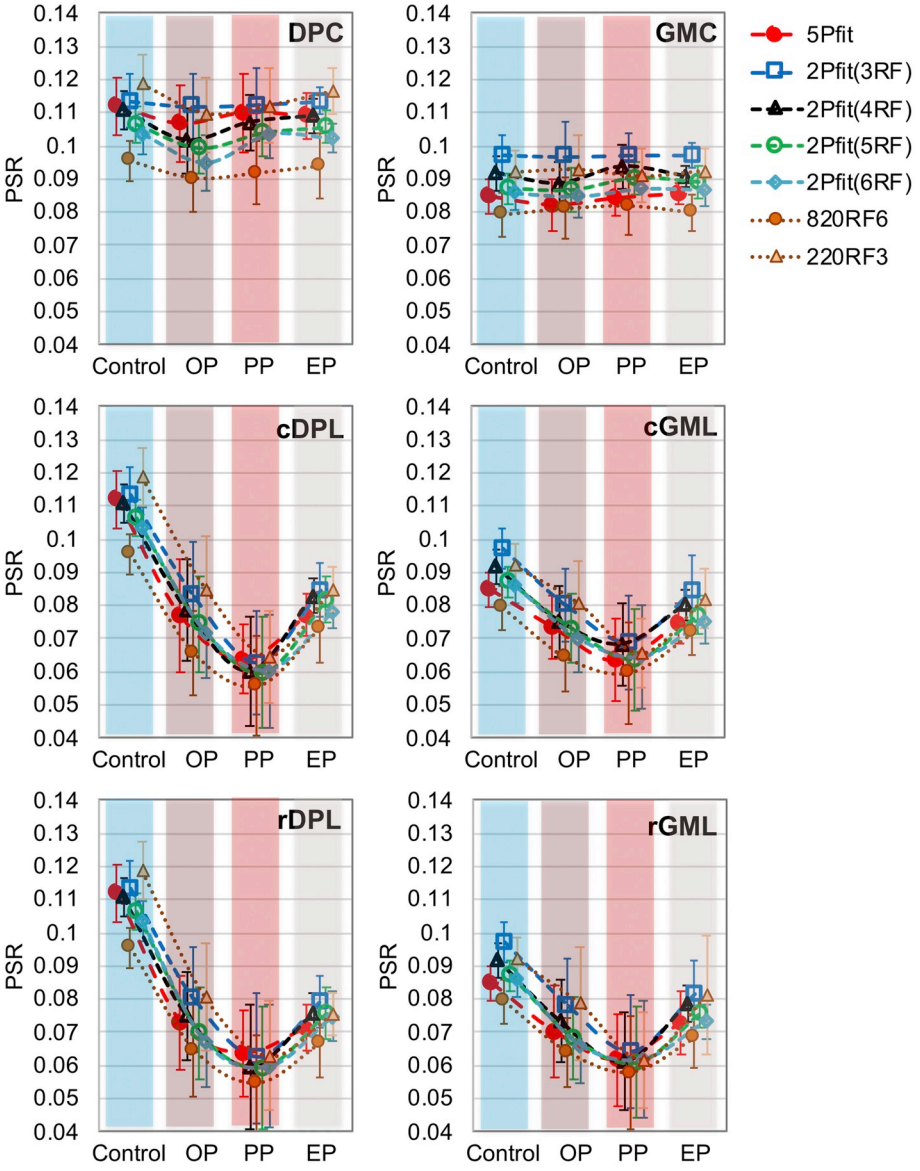

Fig. 10. Longitudinal changes of regional PSR measures across subjects. Progress after injury has been divided into three periods. Selected regions rostral and caudal to the lesion site were compared to the respective control regions. Please see Fig. 6 for ROI definition.

4.3. Alterative simplified approach for PSR mapping of injured spinal cord

The PSR measures from simplified 2-parameter fitting provided comparable sensitivity in assessing lesion-associated damage and recovery (Fig. 7 and Fig. 10) as those from 5-parameter fits. In the experimental data, the precision of PSR from the 2-parameter approach tended to be less variable than those from the 5-parameter approach (RF = 12), across homogeneous tissues, especially when the number of RF offsets used in 2-parameter approaches increased (Fig. 3, Fig. 4, and Fig. 7). Thus 2-parameter fitting can improve the detectability of PSR to injury and recovery (Fig. 7 and Fig. 10). In addition, 2-parameter modeling provided PSR estimates for tissues closer to those from 5-parameter modeling than 1-parameter modeling, even though the estimated *PSR* values obtained with a 2-parameter model tended to be different than those obtained with the 5-parameter model (Fig. 7). The potential for bias in the *PSR* estimates must be balanced with the reductions in scan time, noise sensitivity, and data analysis time that the 2-parameter approach provides. From the above comparisons and considerations, 2Pfit(RF4) is suggested for future simplified approaches for assessing PSR.

4.4. The value of regional PSR in monitoring specific spinal pathology and function

Reliable PSR measures derived from the simplified 2-parameter fitting are of practical significance and have important implications for preclinical and clinical studies that aim to track spinal compartment-specific pathology and function over time, and to relate pathology to specific behavioral impairments. For example, lateral and dorsal WM tracts carry different types of sensory information (temperature, pain, and discriminative touch) to the brain. Disruptions of these two tracts at high and middle cervical level result in various behavioral deficits, including altered temperature and pain sensation, and impaired sensorimotor function of hand (*e.g.*, skilled hand use). Damage to the GM leads to impaired sensory (dorsal horns) and motor behaviors (ventral horns) at the spinal level. Here we showed that a targeted unilateral

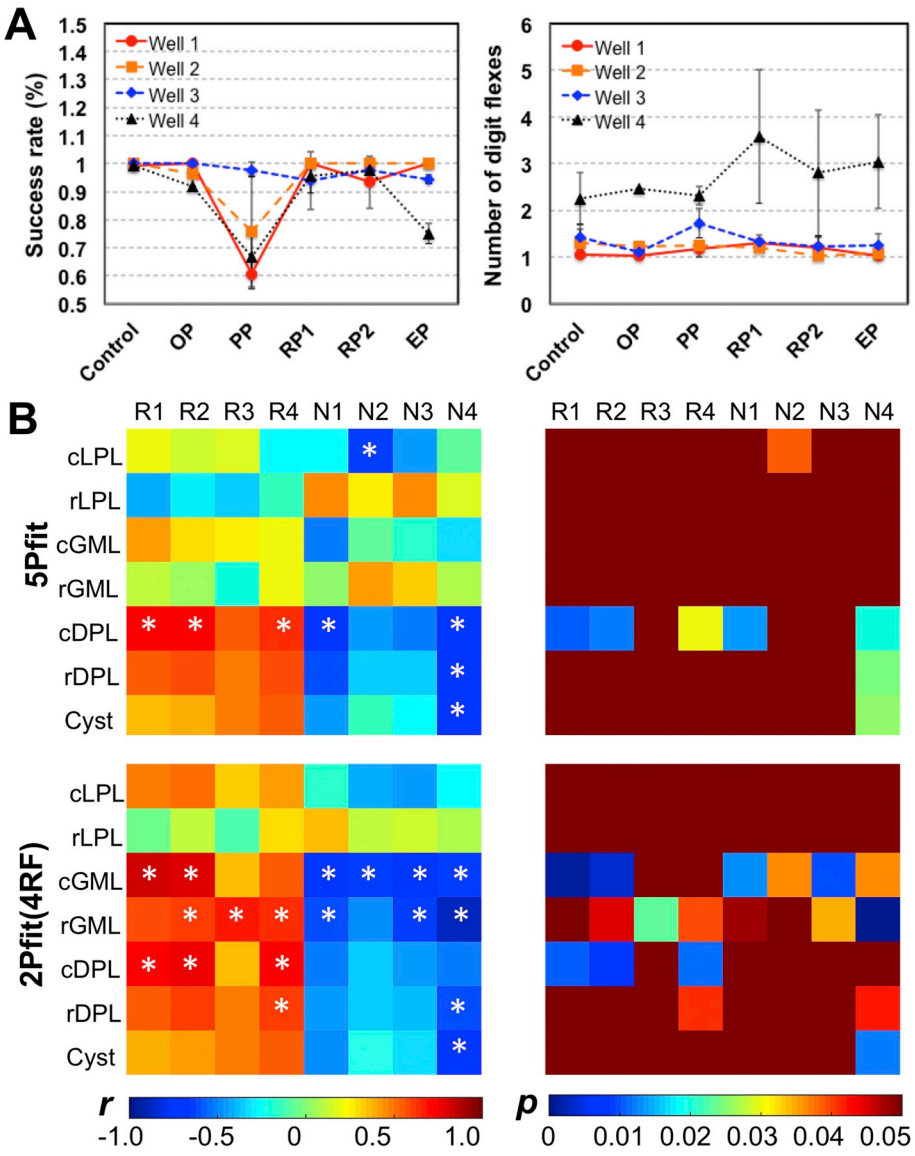

Fig. 11. Relations between longitudinal changes of regional PSR measures and behavioral recovery. (A) Success rate and number of digit flexes show transient behavioral deficits for one representative subject during five post-injury recovery periods (OP, PP, RP1, RP2 and EP) in addition to the pre-lesion control. More time points RP1 and RP2 during the recovery were shown. (B) Correlations between PSR and behavioral measures (n = 4 subjects). Only the time points with both qMT and behavioral measures were included in the correlation analysis. R1-R4: Success rates for well 1–4, respectively. N1-N4: Number of digit flexes for well 1–4, respectively. *p < 0.05.

dorsal column lesion led to decreases of PSR in dorsal WM tracts rostral and caudal to the injury, which likely reflects demyelination and axonal damage induced by trauma. Reduction of PSR in GM (primarily the dorsal horn) of the segments below and above the injury may indicate the loss of neuronal cell bodies, neuropil and glial cells after injury. The GM pathology may interestingly contribute to our previous observations of disrupted functional connectivity between bilateral GM dorsal horns of the below injury segment(Chen et al., 2015). Moreover, our data indicated that over time the cyst shrank, and remyelination of WM and cell regeneration in GM occurred (Figs. 8–10). Importantly these changes in PSR of dorsal WM and GM on the lesion side significantly correlated with behavioral recovery (Fig. 11 and Sup. Fig. S8). Finally, it worth noting that in addition to the dynamic and plastic changes that occurred in the injured spinal cord itself, plasticity in the brain also contributes to the behavioral recovery in this experimental model (Chen et al., 2012; Qi et al., 2016). Together, top-down influences from the brain may explain the discrepancy of the fully recovered behavior of hand uses, but only partial recovery of the injured spinal cord structures 2–6 months after SCI (Figs. 8–10) and the functional connectivity reported in our previous study (Chen et al., 2015).

5. Conclusions

An optimum 2-parameter qMT fitting to a simplified model showed comparable detectability as 5-parameter modeling, in mapping demyelination and remyelination of WM around lesion sites, especially in the dorsal pathway on the lesion side, as well as pathology of GM. This study supports the use of the optimized 2-parameter approaches for qMT imaging of injured spinal cord as a means to reduce total imaging time and/or permit additional MRI measures.

Conflict of interest statement

None of the authors have potential conflicts of interest to be disclosed.

Funding

This study is supported by United States Department of Defense grant W81XWH-17-1-0304, and National Institutes of Health grants NS092961 and NS078680.

Acknowledgements

We thank Mr. Ken Wilkens of the Vanderbilt University Institute of Imaging Science (VUIIS) for customizing coils for cervical spinal cord imaging. We thank Mrs. Chaohui Tang and Mr. Fuxue Xin of VUIIS for their assistance in animal preparation and care in MRI data collection. We also thank Dr. Zou Yue of VUIIS for her assistant in behavioral assessment.

Appendix A. Supplementary data

Supplementary data to this article can be found online at https://doi.org/10.1016/j.nicl.2019.101921.

References

Catalaa, I., Grossman, R.I., Kolson, D.L., Udupa, J.K., Nyul, L.G., Wei, L., Zhang, X., Polansky, M., Mannon, L.J., McGowan, J.C., 2000. Multiple sclerosis: magnetization transfer histogram analysis of segmented normal-appearing white matter. Radiology 216 (2), 351–355.

Cercignani, M., Alexander, D.C., 2006. Optimal acquisition schemes for in vivo quantitative magnetization transfer MRI. Magn. Reson. Med. 56 (4), 803–810.

Cercignani, M., Barker, G.J., 2008. A comparison between equations describing in vivo MT: the effects of noise and sequence parameters. J. Magn. Reson. 191 (2), 171–183.

Chen, L.M., Qi, H.X., Kaas, J.H., 2012. Dynamic reorganization of digit representations in somatosensory cortex of nonhuman primates after spinal cord injury. J. Neurosci. 32 (42), 14649–14663.

Chen, L.M., Mishra, A., Yang, P.F., Wang, F., Gore, J.C., 2015. Injury alters intrinsic functional connectivity within the primate spinal cord. Proc. Natl. Acad. Sci. U. S. A. 112 (19), 5991–5996.

Eng, J., Ceckler, T.L., Balaban, R.S., 1991. Quantitative 1H magnetization transfer imaging in vivo. Magn. Reson. Med. 17 (2), 304–314.

Gochberg, D.F., Gore, J.C., 2003. Quantitative imaging of magnetization transfer using an inversion recovery sequence. Magn. Reson. Med. 49 (3), 501–505.

Guest, J.D., Hiester, E.D., Bunge, R.P., 2005. Demyelination and Schwann cell responses adjacent to injury epicenter cavities following chronic human spinal cord injury. Exp. Neurol. 192 (2), 384–393.

Henkelman, R.M., Huang, X.M., Xiang, Q.S., Stanisz, G.J., Swanson, S.D., Bronskill, M.J., 1993. Quantitative interpretation of magnetization-transfer. Magn. Reson. Med. 29 (6), 759–766.

Kaas, J.H., Qi, H.X., Burish, M.J., Gharbawie, O.A., Onifer, S.M., Massey, J.M., 2008. Cortical and subcortical plasticity in the brains of humans, primates, and rats after damage to sensory afferents in the dorsal columns of the spinal cord. Exp. Neurol. 209 (2), 407–416.

Li, K., Dortch, R.D., Kroop, S.F., Huston, J.W., Gochberg, D.F., Park, J.H., Damon, B.M., 2015. A rapid approach for quantitative magnetization transfer imaging in thigh muscles using the pulsed saturation method. Magn. Reson. Imaging 33 (6), 709–717.

McGowan 3rd, J.C., Schnall, M.D., Leigh, J.S., 1994. Magnetization transfer imaging with pulsed off-resonance saturation: variation in contrast with saturation duty cycle. J. Magn. Reson. Imaging 4 (1), 79–82.

Ng, M.C., Hua, J., Hu, Y., Luk, K.D., Lam, E.Y., 2009. Magnetization transfer (MT) asymmetry around the water resonance in human cervical spinal cord. J. Magn. Reson. Imaging 29 (3), 523–528.

Odrobina, E.E., Lam, T.Y., Pun, T., Midha, R., Stanisz, G.J., 2005. MR properties of excised neural tissue following experimentally induced demyelination. NMR Biomed. 18 (5), 277–284.

Qi, H.X., Chen, L.M., Kaas, J.H., 2011. Reorganization of somatosensory cortical areas 3b and 1 after unilateral section of dorsal columns of the spinal cord in squirrel monkeys. J. Neurosci. 31 (38), 13662–13675.

Qi, H.X., Wang, F., Liao, C.C., Friedman, R.M., Tang, C., Kaas, J.H., Avison, M.J., 2016. Spatiotemporal trajectories of reactivation of somatosensory cortex by direct and secondary pathways after dorsal column lesions in squirrel monkeys. Neuroimage 142, 421–443.

Quesson, B., Bouzier, A.K., Thiaudiere, E., Delalande, C., Merle, M., Canioni, P., 1997. Magnetization transfer fast imaging of implanted glioma in the rat brain at 4.7 T: interpretation using a binary spin-bath model. J. Magn. Reson. Imaging 7 (6), 1076–1083.

Ramani, A., Dalton, C., Miller, D.H., Tofts, P.S., Barker, G.J., 2002. Precise estimate of fundamental in-vivo MT parameters in human brain in clinically feasible times. Magn. Reson. Imaging 20 (10), 721–731.

Sled, J.G., Pike, G.B., 2000. Quantitative interpretation of magnetization transfer in spoiled gradient echo MRI sequences. J. Magn. Reson. 145 (1), 24–36.

Sled, J.G., Pike, G.B., 2001. Quantitative imaging of magnetization transfer exchange and relaxation properties in vivo using MRI. Magn. Reson. Med. 46 (5), 923–931.

Smith, S.A., Golay, X., Fatemi, A., Mahmood, A., Raymond, G.V., Moser, H.W., van Zijl, P.C., Stanisz, G.J., 2009. Quantitative magnetization transfer characteristics of the human cervical spinal cord in vivo: application to adrenomyeloneuropathy. Magn. Reson. Med. 61 (1), 22–27.

Smith, A.K., Dortch, R.D., Dethrage, L.M., Smith, S.A., 2014. Rapid, high-resolution quantitative magnetization transfer MRI of the human spinal cord. Neuroimage 95, 106–116.

Stroman, P.W., Wheeler-Kingshott, C., Bacon, M., Schwab, J.M., Bosma, R., Brooks, J., Cadotte, D., Carlstedt, T., Ciccarelli, O., Cohen-Adad, J., Curt, A., Evangelou, N., Fehlings, M.G., Filippi, M., Kelley, B.J., Kollias, S., Mackay, A., Porro, C.A., Smith, S., Strittmatter, S.M., Summers, P., Tracey, I., 2014. The current state-of-the-art of spinal cord imaging: methods. NeuroImage 84, 1070–1081.

Thuret, S., Moon, L.D., Gage, F.H., 2006. Therapeutic interventions after spinal cord injury. Nat. Rev. Neurosci. 7 (8), 628–643.

Totoiu, M.O., Keirstead, H.S., 2005. Spinal cord injury is accompanied by chronic progressive demyelination. J. Comp. Neurol. 486 (4), 373–383.

Underhill, H.R., Rostomily, R.C., Mikheev, A.M., Yuan, C., Yarnykh, V.L., 2011. Fast bound pool fraction imaging of the in vivo rat brain: association with myelin content and validation in the C6 glioma model. Neuroimage 54 (3), 2052–2065.

Wang, F., Jiang, R., Takahashi, K., Gore, J., Harris, R.C., Takahashi, T., Quarles, C.C., 2014. Longitudinal assessment of mouse renal injury using high-resolution anatomic and magnetization transfer MR imaging. Magn. Reson. Imaging 32 (9), 1125–1132.

Wang, F., Qi, H.X., Zu, Z., Mishra, A., Tang, C., Gore, J.C., Chen, L.M., 2015. Multiparametric MRI reveals dynamic changes in molecular signatures of injured spinal cord in monkeys. Magn. Reson. Med. 74 (4), 1125–1137.

Wang, F., Li, K., Mishra, A., Gochberg, D., Chen, L.M., Gore, J.C., 2016. Longitudinal assessment of spinal cord injuries in nonhuman primates with quantitative magnetization transfer. Magn. Reson. Med. 75 (4), 1685–1696.

Wang, F., Katagiri, D., Li, K., Takahashi, K., Wang, S.W., Nagasaka, S., Li, H., Quarles, C.C., Zhang, M.Z., Shimizu, A., Gore, J.C., Harris, R.C., Takahashi, T., 2018a. Assessment of renal fibrosis in murine diabetic nephropathy using quantitative magnetization transfer MRI. Magn. Reson. Med. 80 (6), 2655–2669.

Wang, F., Zu, Z.L., Wu, R.Q., Wu, T.L., Gore, J.C., Chen, L.M., 2018b. MRI evaluation of regional and longitudinal changes in Z-spectra of injured spinal cord of monkeys. Magn. Reson. Med. 79 (2), 1070–1082.

Wheeler-Kingshott, C.A., Stroman, P.W., Schwab, J.M., Bacon, M., Bosma, R., Brooks, J., Cadotte, D.W., Carlstedt, T., Ciccarelli, O., Cohen-Adad, J., Curt, A., Evangelou, N., Fehlings, M.G., Filippi, M., Kelley, B.J., Kollias, S., Mackay, A., Porro, C.A., Smith, S., Strittmatter, S.M., Summers, P., Thompson, A.J., Tracey, I., 2014. The current state-of-the-art of spinal cord imaging: applications. NeuroImage 84, 1082–1093.

Wolff, S.D., Balaban, R.S., 1989. Magnetization transfer contrast (MTC) and tissue water proton relaxation in vivo. Magn. Reson. Med. 10 (1), 135–144.

Wolff, S.D., Chesnick, S., Frank, J.A., Lim, K.O., Balaban, R.S., 1991a. Magnetization transfer contrast: MR imaging of the knee. Radiology 179 (3), 623–628.

Wolff, S.D., Eng, J., Balaban, R.S., 1991b. Magnetization transfer contrast: method for improving contrast in gradient-recalled-echo images. Radiology 179 (1), 133–137.

Yang, P.F., Wang, F., Chen, L.M., 2015. Differential fMRI activation patterns to noxious heat and tactile stimuli in the primate spinal cord. J. Neurosci. 35 (29), 10493–10502.

Yarnykh, V.L., 2012. Fast macromolecular proton fraction mapping from a single off-resonance magnetization transfer measurement. Magn. Reson. Med. 68 (1), 166–178.

Yarnykh, V.L., Yuan, C., 2004. Cross-relaxation imaging reveals detailed anatomy of white matter fiber tracts in the human brain. Neuroimage 23 (1), 409–424.